Bendable Aqueous Zinc-Ion Hybrid Energy Storage Device Using Poly(4,4'-thiodianiline)-Modified Nanoporous Carbon Cathode

Tuo Xin,[a] Qiuju Xu,[a] Xiangcheng Yuan,[a] Qi Zhang,[a] Meinan Liu,[b] and Jinzhang Liu*[a]

The Zn^{2+} based battery systems have attracted considerable interest because of the bivalent ions as charge carriers and merits of Zn anode. Herein, we demonstrate a Zn-ion hybrid energy storage device consisting of a Zn anode and a cathode made of poly(4,4'-thiodianiline)-coated activated carbon (AC). This redox-active polymer that is electrodeposited onto nanoporous AC granules has the function of boosting the energy storage capacity, reaching $181.3\ mAh\,g^{-1}$. The Zn-ion cell exhibits good cycling stability, as the capacity retention is 83% after 5000 cycles. Aqueous electrolytes using different zinc salts are prepared and their influences on the formation of by-products and cycling stability of the cell are investigated. The charge/discharge mechanism of the polymer cathode is discussed in detail. Moreover, for practical applications, bending tests are performed on the flexible Zn-ion cell, and it remains stable capacity when being repeatedly bent.

Introduction

Technologies in portable electronics and electric vehicles have progressed rapidly over the past decade, and robust energy storage devices are now in urgent need. Currently, electrochemical energy storage devices such as Li/Na ion batteries,[1,2] alkaline Zn/MnO_2 batteries,[3] Li–S batteries,[4] and supercapacitors[5] are being intensively studied. Supercapacitors that rely on physical adsorption of ions for charge storage have high power density, long cycling life, and high safety, yet a major drawback is the low energy density.[6] Secondary batteries are charged/discharged via reversible chemical reactions and normally have much higher energy densities than supercapacitors, but suffer from low power capability and unsatisfactory cycling life. Therefore, it is of great interest to develop hybrid energy storage devices that combine merits of both supercapacitors and ionic batteries. Aqueous supercapacitors or batteries have advantages of high safety, low cost, and high kinetics compared to their counterparts using organic electrolytes. Because the water splitting voltage is ~1.23 V, asymmetric supercapacitors using two dissimilar electrode materials were designed to broaden the voltage window even beyond 2 V.[7] Also, Li-, Na- or K-ion hybrid supercapacitors using organic electrolytes were reported.[8–11] Those cells can be charged up to 4 V, attributed to the combination of asymmetric design and organic electrolyte.

Multivalent metal ions such as Zn^{2+}, Mg^{2+}, and Al^{3+} are superior to alkali metal ions in developing safer and better batteries. The use of Zn anode and nanoporous carbon cathode to make aqueous hybrid supercapacitors were recently reported.[12–14] Yang et al. fabricated degradable rechargeable Zn//MXene capacitors which showed excellent anti-self-discharge function.[15] As an extension of Zn-ion capacitors, researchers have also developed photo-charged Zn-ion capacitors by introducing photoactive electrode materials such as V_2O_5 or g-C_3N_4.[16,17] The cathode materials of Zn-ion capacitors/batteries play a key role in enhancing the energy storage capacity. Pseudocapacitive materials, including transition metal oxides,[18] conducting polymers,[19] and some aromatic molecules,[20] generally exhibit much higher specific capacitance than porous carbonaceous materials. In particular, organic electrode materials are light weight, flexible, and diverse in molecular structure.[21–24] Therefore, redox-active polymers provide a rich source for sorting out appropriate cathode materials of Zn-ion electrochemical energy storage devices.

Here, for the first time, we report an organic cathode material, poly(4,4'-thiodianiline, TDA), for making aqueous Zn-ion hybrid energy storage device. This polymer was electrodeposited onto nanoporous activated carbon (AC) coatings to boost the charge storage capacity. The flat cells are bendable and can be operated within a wide voltage window of 0.2–1.8 V. The effects of different Zn salts in aqueous electrolyte on the formation of byproducts and cycling stability were investigated in detail.

Results and Discussion

The scanning electron microscopy (SEM) image in Figure 1(a) depicts the morphology of carbon fiber cloth used as current collector for cathode. A slurry containing nanoporous AC, black

[a]   Dr. T. Xin, Dr. Q. Xu, Dr. X. Yuan, Q. Zhang, Prof. J. Liu
      School of Materials Science and Engineering
      Beihang University
      Beijing 100083, China
      E-mail: ljz78@buaa.edu.cn
[b]   Prof. M. Liu
      Suzhou Institute of Nano-Tech and Nano-Bionics
      Chinese Academy of Sciences
      Suzhou 215123, China

Batteries & Supercaps

Research Article
doi.org/10.1002/batt.202100318

Chemistry Europe
European Chemical
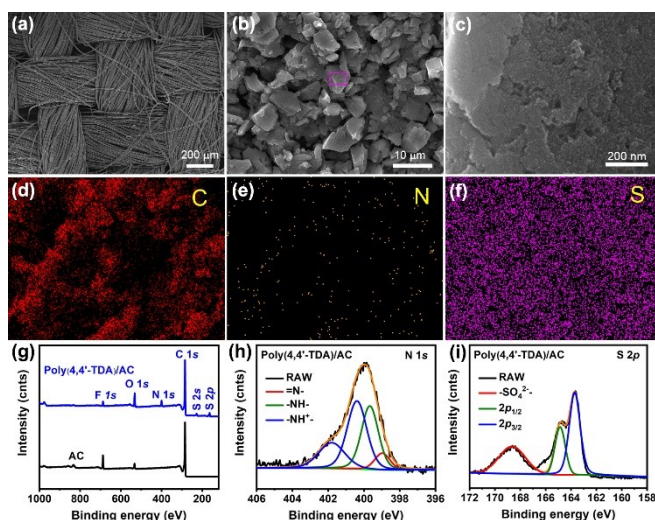Societies Publishing

Figure 1. a) SEM image of the carbon fiber cloth used as current collector. b) SEM image of a typical poly(4,4'-TDA)/AC cathode. A close-view image on a single granule of this sample is shown in c). d–f) C, N, and S elemental mappings from the same area as in (c), respectively. g) Survey XPS spectra of a poly(4,4'-TDA)/AC cathode and a bare AC coating. h and i) High-resolution XPS N 1s and S 2p spectra of the cathode, respectively.

carbon, and polyvinylidene difluoride at a weight ratio of 8:1:1 was coated onto the carbon cloth, followed by a drying process. After the electrodeposition of poly(4,4'-TDA) on AC coating, the cathode morphology was further examined by SEM, as shown in Figure 1(b). A close-view SEM image of a single AC granule coated with poly(4,4'-TDA) is shown in Figure 1(c). The nanopores of AC are believed to be filled with polymer molecules, because the AC product with higher specific surface also led to higher capacity after electrodeposition of poly(4,4'-TDA). Here, the AC powder with specific surface area of $2280 \, m^2 \, g^{-1}$ was used. Figure 1(d–f) show elemental mappings for C, N, and S distributions over the same area as in Figure 1(c), respectively. The signals of N and S confirm the presence of poly(4,4'-TDA). In addition, X-ray photoelectron microscopy (XPS) was employed to study the surface chemistry of the poly(4,4'-TDA)/AC cathode. The two survey spectra of bare AC and poly(4,4'-TDA)/AC are compared in Figure 1(g). Both show F 1s, C 1s, and O 1s peaks. The F 1s signal comes from the polyvinylidene difluoride binder. The poly(4,4'-TDA)/AC cathode shows additional N and S signals from the electrodeposited polymer, which is in agreement with our elemental mapping analysis. The high-resolution N 1s XPS spectrum in Figure 1(h) is fitted by four peaks with binding energies at 398.9, 399.6, 400.3 and 401.7 eV, corresponding to imine ($=N-$), amine ($-NH-$) and positively charged amine ($-NH^+-$, >400 eV), respectively. As for the S 2p XPS spectrum in Figure 1(i), sub-peaks of S $2p_{3/2}$ at 163.7 eV and S $2p_{1/2}$ at 164.8 eV are dicernible. The borad peak centered at 168.5 eV is related to S–O bonds.[25]

To investigate the electrochemical performance of the poly(4,4'-TDA)/AC cathode, sandwich-structured cells were assembled by using the Zn foil anode and the poly(4,4'-TDA)/AC cathode. The in-between separator was a glass fiber

membrane soaked with aqueous electrolyte. The device was encapsulated into a flat pouch made of aluminum-plastic film for electrochemical tests (Figure S3). Different zinc salts, including $ZnSO_4$, $Zn(CF_3SO_3)_2$, and $ZnCl_2$, have used to make aqueous electrolytes for Zn-ion batteries.[26,27] The used of $ZnCl_2$ electrolyte normally results in a narrower voltage window due to the evolution of Cl_2, and this electrolyte is not suitable for our polymer cathode, according to the cyclic voltammetry (CV) loops (Figure S9). CV loops of our cathode tested in $ZnSO_4$ and $Zn(CF_3SO_3)_2$ electrolytes, respectively, exhibited distinct redox peaks and were nearly identical in shape, as shown in Figure S10(a). To determine the appropriate electrolyte for our cathode, we tested three electrolytes, i.e., $ZnSO_4$, $Zn(CF_3SO_3)_2$, and the mixture of $ZnSO_4$ and $Zn(CF_3SO_3)_2$ at molar ratio of 1:1. The three electrolytes were identical in Zn^{2+} concentration, as 2 M. As shown in Figure 2(a), the cycling stability of our poly(4,4'-TDA)/AC cathode is strongly dependent on the electrolyte. The cell using $ZnSO_4$ electrolyte showed the best cycling performance. The use of $Zn(CF_3SO_3)_2$ electrolyte led to severe capacity decay during the cycling process. When using the mixture solution of $ZnSO_4$ and $Zn(CF_3SO_3)_2$, the cycling performance was much improved, compared to the sole use of $Zn(CF_3SO_3)_2$. Hence, we conclude that the $ZnSO_4$ electrolyte is the appropriate one for our cathode. Although the molecular structure of a 4,4'-TDA monomer is symmetrical (Figure S4), the structural geometry of poly(4,4'-TDA) is believed to be
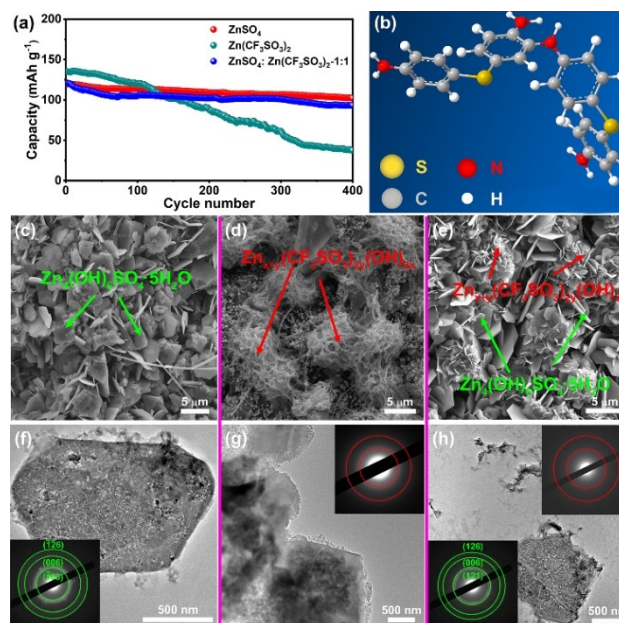

Figure 2. a) Cycling performance of three Zn//poly(4,4'-TDA)/AC cells with different electrolytes. b) Molecular structure of poly(4,4'-TDA). c and f) Typical TEM images of poly(4,4'-TDA)/AC cathode after cycling in $ZnSO_4$ electrolyte. Inset in (f) is the corresponding SAED pattern of $Zn_4(OH)_6SO_4 \cdot 5H_2O$. d and g) Typical TEM images of poly(4,4'-TDA)/AC cathode after cycling in $Zn(CF_3SO_3)_2$ electrolyte. Inset in (g) is the corresponding SAED pattern of $Zn_{x+y}(CF_3SO_3)_{2x}(OH)_{2y}$. e and h) Typical TEM images of poly(4,4'-TDA)/AC cathode after cycling in $ZnSO4:Zn(CF_3SO_3)_2$-1:1 electrolyte. The upper-right corner inset shows the corresponding SAED pattern of $Zn_{x+y}(CF_3SO_3)_{2x}(OH)_{2y}$ and the lower-left corner inset shows the corresponding SAED pattern of $Zn_4(OH)_6SO_4 \cdot 5H_2O$.

entangled. For instance, Figure 2(b) shows the spatial structure of a relaxed 4,4'-TDA dimer, which is naturally twisted. It is conceivable that some inserted ions in the polymer cathode could be stuck entangled molecular chains and subsequently block the diffusion path for insertion and deinsertion of ions in the following charge-discharge process, thus causing capacity decay. Since $CF_3SO_3^-$ is large than SO_4^{2-}, $CF_3SO_3^-$ ions are easier to be stuck in the polymer cathode and prone to cause capacity decay. The ion conductivities of the three electrolytes were measured to be 208, 165, and 178 mS cm^{-1} for $ZnSO_4$, Zn-$(CF_3SO_3)_2$, and the mixture of the two with equal molar fraction. A high ion conductivity of the electrolyte favors the power capability and rate performance of the cell. Therefore, for our poly(4,4'-TDA)/AC cathode the inexpensive $ZnSO_4$ electrolyte is the optimal choice.

For aqueous ZIBs, byproducts are normally inevitable due to parasitic reactions. Figure 2(c–e) show SEM images of the poly(4,4'-TDA)/AC cathode after being cycled at 8 mA cm^{-2} for 400 cycles in the three different electrolytes. When charged/discharged in a pure $ZnSO_4$ electrolyte, flake-shaped byproducts were formed. However, the use of pure $Zn(CF_3SO_3)_2$ electrolyte led to the formation of nanosheet networks as byproduct. The flake byproduct in $ZnSO_4$ electrolyte can be identified as $Zn_4(OH)_6SO_4 \cdot 5H_2O$, according to previous reports.[13] Transmission electron microscopy (TEM) images of the byproducts in $ZnSO_4$, $Zn(CF_3SO_3)_2$, and mixture solution of the two salts are shown in Figures 2(f and g), and 3(h), respectively. In Figure 2(f), the selected-area electron diffraction (SAED) pattern as an inset can be indexed to $Zn_4(OH)_6SO_4 \cdot 5H_2O$. For the SAED image in Figure 2(g), neither spots nor bright rings can be found, indicating the amorphous feature of the byproduct identified as $Zn_{x+y}(CF_3SO_3)_{2x}(OH)_{2y}$.[28]

For the byproduct formed in the mixture solution of $ZnSO_4$ and $Zn(CF_3SO_3)_2$ (molar ratio 1:1), it contains both crystalline $Zn_4(OH)_6SO_4 \cdot 5H_2O$ and amorphous $Zn_{x+y}(CF_3SO_3)_{2x}(OH)_{2y}$, as indicated by the two SAED patterns in Figure 2(h).

For a typical cell with AC mass loading of 3.7 mg cm^{-2} in the cathode, its CV loops within the voltage range of 0.2–1.8 V and at different voltage scan rates are shown in Figure 3(a). Note that the mass loading of cathode was increased by 30 - 50%, depending on the areal mass loading of AC, after the electrodeposition of poly(4,4'-TDA), . The polymer cathode exhibited a pair of redox peaks over the CV loop, and the separation between oxidation and reduction peaks were widened due to electric polarization. For comparison, CV loops from a Zn||AC cell, also named hybrid supercapacitor, measured within the voltage range of 0.2–1.8 V and at different voltage scan rates are shown in Figure S7. Except for the weak redox peaks contributed by oxygenated groups in AC, the CV loops are quasi-rectangular. In principle, the relationship between redox peak current (i) and potential scan rate (ν) can be expressed as $i = a\nu^b$, where a and b are adjustable parameters.[14] When the b-value is close to 0.5, the reaction process relies on ionic diffusion control. However, when the b-value is 1, the reaction represents a capacitive behavior. As shown in Figure S6, the b-values calculated from the curves of log (i) versus log (ν) for peaks 1 and 2 are 0.82 and 0.89, respectively. These high b-values indicate that the kinetics of Zn^{2+} in the poly(4,4'-TDA)/AC cathode are more like surface-controlled pseudocapacitance. Furthermore, from 2 to 10 mV s^{-1}, the capacitive contribution to the overall charge storage process was increased from 67% to 83%, favoring the rate performance.
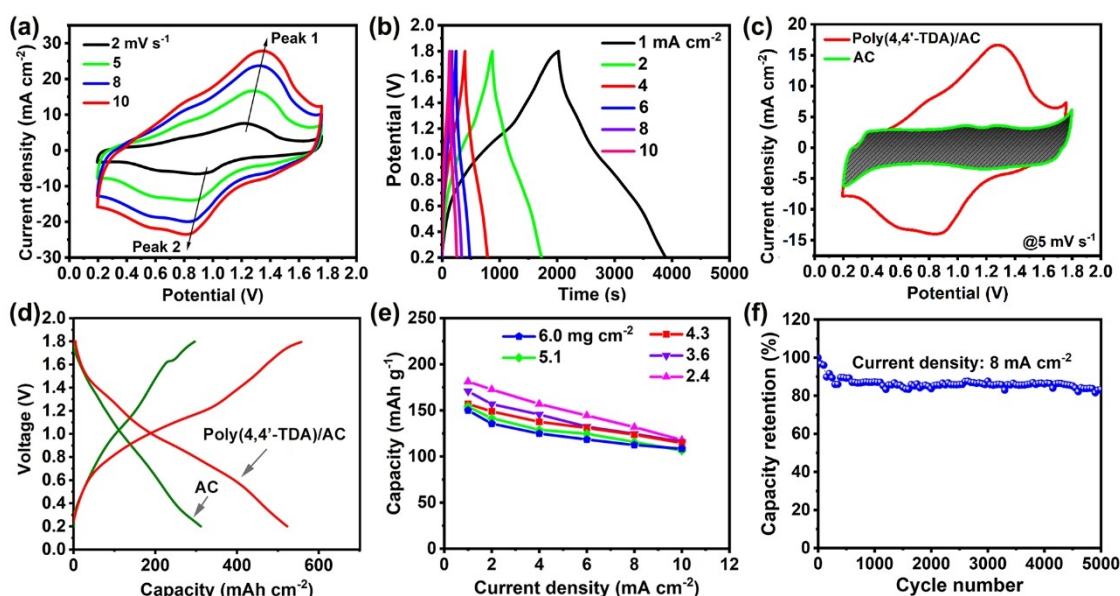

Figure 3. a) CV curves of the Zn//poly(4,4'-TDA)/AC cell at different sweep rates from 2 to 10 mV s^{-1}. b) GCD curves of the cell at different current densities. c) Two CV loops collected from a Zn//poly(4,4'-TDA)/AC cell and a Zn//AC cell with identical AC mass loading in the cathode, respectively. d) GCD curves of the two devices. e) Gravimeric capacities over the current density for several Zn//poly(4,4'-TDA)/AC cells with different AC mass loadings in the cathode. f) Cycling stability of a typical Zn//poly(4,4'-TDA)/AC cell.

Galvanostatic charge/discharge (GCD) curves of the Zn||poly(4,4'-TDA)/AC cell at different current densities ranging from 2 to 10 mA cm^{-2} are shown in Figure 3(b). The shape of a GCD curve is nearly triangular, which resembles that of electric double-layer supercapacitor. Figure 3(c) shows two CV loops at 5 mV s^{-1} collected from a Zn//poly(4,4'-TDA)||AC cell and a Zn||AC cell, respectively. Both have identical AC mass loadings in the cathode. The area of a CV loops is related to the charge storage capacity. Hence, it is evident that the introduction of poly(4,4'-TDA) to AC can largely enhance the charge storage capacity. For further comparison, charge/discharge curves at 1 mA cm^{-2} from the Zn||poly(4,4'-TDA)/AC cell and the Zn||AC cell are shown in Figure 3(d). The discharge capacities of poly(4,4'-TDA)/AC and bare AC cathodes are 524 and 311 mAh cm^{-2}, respectively. Because the mass loading of cathode play a key role in specific capacitance, we prepared poly(4,4'-TDA)/AC cathodes with different AC mass loadings ranging from 2.4 to 6.0 mg cm^{-2}. Gravimetric capacities of these cathodes at different discharge current densities are shown in Figure 3(e). Apparently, the lower the mass loading of cathode material, the higher the gravimetric capacity. For the cell with the thinnest cathode coating, the gravimetric capacity reached 181.3 mAh g^{-1} at 1 mA cm^{-2}. With increasing the discharge current to 10 mA cm^{-2}, the capacity was gradually decreased to 117.8 mAh g^{-1}, corresponding to a capacity retention of 65%. The good rate performance of this cell can be attributed to the fast reaction kinetics of the Faradaic process. Correspondingly, areal capacities of these cathodes are shown in Figure S8. The

highest areal capacity reached 0.91 mAh cm^{-2}. The cycling stability is an important issue for evaluating the device. In Figure 3(f), the device after continuously charged and discharged at 8 mA cm^{-2} for 5000 cycles showed a capacity retention of 83%. Our SEM observation on a Zn foil anode after 5000 cycles revealed that densely packed thin flakes, instead of zinc dendrites, were grown out over the anode surface, as seen in Figure S12. Presumably, the corrosion of Zn foil is partially responsible for the capacity decay after long-term cycling test, as the exposed surface area of Zn anode is reduced due to the coverage of byproducts.

With the fast development of wearable electronics, flexible energy storage devices have received much attention.[29] Since our Zn||poly(4,4'-TDA)/AC cell in a flat pouch is bendable, the influence of mechanical bending on the energy storage performance was studied, as shown in Figure 4(a). The cell was repeatedly bent and released with running the cycling test. During the cycling process, the nearly 100% Coulombic efficiency rules out the water decomposition inside the cell when charged to 1.8 V. The Ragone plots in Figure 4(b), collected from a group of Zn||poly(4,4'-TDA)/AC cells with different AC mass loadings in the cathode, show a maximum energy density of 0.73 mWh cm^{-2}, which corresponds to 203 Wh kg^{-1}, from the device with the lowest AC mass loading of 2.4 mg cm^{-2}. The power densities of these cells are in the range of 0.8–9 mW cm^{-2} (or 0.2–2.5 kW kg^{-1}). It should be addressed that the energy density of our device is higher than those of other aqueous asymmetric supercapacitors that were
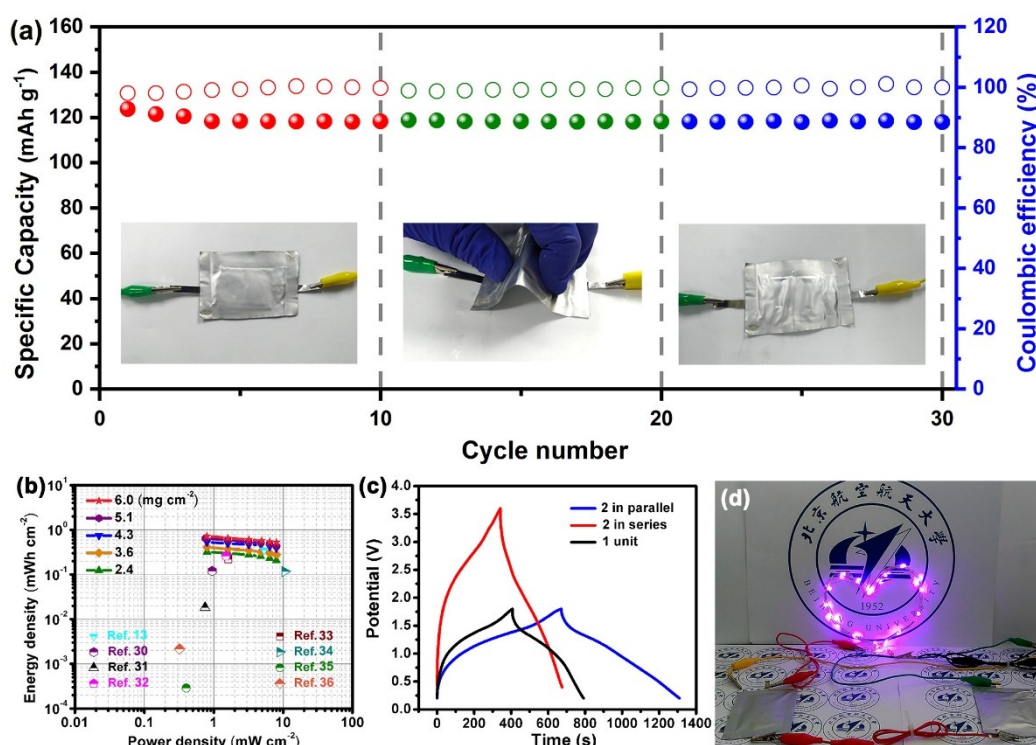

Figure 4. a) Cycling stability of a flexible Zn||poly(4,4'-TDA)/AC cell being bent and flattened by hand. b) Ragone plots of a group of Zn||poly(4,4'-TDA)/AC cells with different AC mass loadings in the cathode. Energy and power densities of other asymmetric supercapacitors in the literature are marked for comparison. c) GCD curves collected from a single cell, two cells connected in series and in parallel, respectively. d) Photograph of a string of violet LEDs lit up by two Zn-ion pouch cells in series.

Batteries & Supercaps

Research Article
doi.org/10.1002/batt.202100318

Chemistry Europe
European Chemical
Societies Publishing

previously reported,[13,30–36] as marked in Figure 4(b). More comparisons between our device and others can be found in Table S1. To meet various applications, several cells may be connected either in series to boost the voltage or in parallel to multiply the capacity. In Figure 4(c), three CD curves at $4\,mA\,cm^{-2}$ are compared. The time span of the CD cycle from two cells in parallel is much wider than that of a single cell, indicating enhanced capacity by the parallel connection. For the CD curve of two cells in series, the voltage window is doubled, compared to that of a single cell. To demonstrate a practical application, two cells in series were used to light up a string of violet LEDs, as shown in Figure 4(d).

Now we look into the charge storage mechanism. Two pouch cells after 100 GCD cycles were dissembled for examination. The two cells being cycled were terminated at different states, i.e., fully charged at 1.8 V or fully discharged at 0.2 V. Each cathode was rinsed using deionized water and then dried for XPS measurement. Figure 5(a) shows the survey XPS spectrum of the discharged cathode, in which the Zn signal is emerged. The high-resolution Zn 2p XPS spectrum is shown in Figure 5(b). The deconvolution of Zn 2p peaks in Figure 5b gives two components at a ratio of 3:1, in agreement with

$Zn_4SO_4(OH)_6 \cdot 5H_2O$.[37,38] This complex Zn compound is formed via the reaction:[13]

$$4Zn^{2+} + 6OH^- + SO_4^{2-} + 5H_2O \rightarrow Zn_4SO_4(OH)_6 \cdot 5H_2O$$
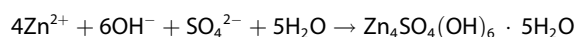
As illustrated in Figure 5(e), the newly assembled cell has an initial open voltage of 1.2 V, because the freshly electro-deposited poly(4,4'-TDA) is at oxidation state, represented by $=NH^+$ groups. During the discharging process, cations like Zn^{2+} and H^+ would move toward the cathode and interact with poly(4,4'-TDA) molecules. $-NH-$ and $=NH^+$ groups are reduced to be $-N^-$ and $-NH_2$, respectively, by inserted cations. The two high-resolution S 2p XPS spectra in Figure 5(b and c) correspond to the discharged and charged cathodes, respectively. The S signal is contributed by both the S in poly(4,4'-TDA) molecule and the flake-shaped byproduct that contains SO_4^{2-}. Also, survey XPS spectra of the poly(4,4'-TDA)/AC cathode at charged/discharged states after being cycled in 2 M Zn-$(CF_3SO_3)_2$ electrolyte were collected, as shown in Figure S10(b). The Zn signal from the cathode at discharged state is stronger than that at charged state, because the complex Zn compound was formed at discharged state, and partially dissolved at charged state due to the local decrease of pH value at the
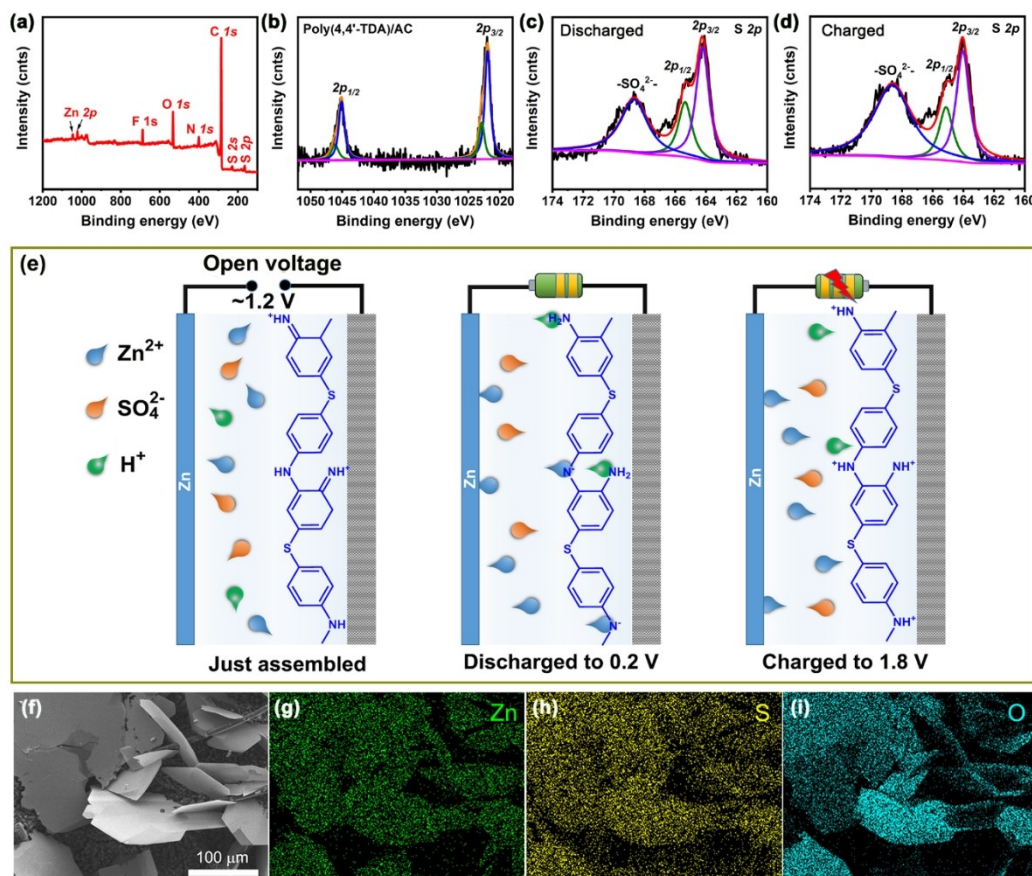

Figure 5. a) Survey XPS spectrum and b) the high-resolution Zn 2p XPS spectrum of poly(4,4'-TDA)/AC cathode after 100 cycles. c and d) S 2p XPS spectra of two cathodes after 100 cycles, ended at discharged and charged states, respectively. e) Proposed energy storage mechanism of the Zn//poly(4,4'-TDA)/AC cell using ZnSO$_4$ electrolyte. f) SEM image of byproduct flakes over the cathode surface after 5000 cycles. g–i) Zn, S, and O elemental mappings of the Zn compound flakes, respectively.

interface. This can be explained by the extraction of H^+ from the cathode in the charging process, as illustrated in Figure 5(e). To verify the role of H^+ in the redox process, we collected CV loops from of the poly(4,4'-TDA)/AC cathode in a three-electrode cell filled with 2 M H_2SO_4, as shown in Figure S11. A Pt foil was used as counter electrode and the reference electrode was Ag/AgCl. The redox peaks over CV loop suggest the reversible reactions between protons and poly(4,4'-TDA) molecules.

The movement of cations and anions in opposite directions promotes the formation of flake-shaped byproducts over both anode and cathode surfaces. The SEM image in Figure S12 depicts the surface of a Zn anode after long-term cycling test. Densely packed flakes were observed. Over the cathode surface, at early stage of the cycling process, the formation and dissolution of flake byproduct are reversible. Figure S13(a and c) shows SEM images of the poly(4,4'-TDA)/AC cathode at discharged and charged states, respectively. Flakes with an average size of ~5 μm were emerged over the cathode surface after being discharged to 0.2 V (Figure S13a). Our EDS mappings for C, S, and Zn elements from this discharged cathode are shown in Figure S13(b). After being charged to 1.8 V, most of these flakes were disappeared, as shown in Figure S13(c). Correspondingly, EDS mappings for Zn, C, and S elements in this discharged cathode are shown in Figure S10(d). It can be seen that Zn signals were barely detected. The dissolution of $Zn_4SO_4(OH)_6 \cdot 5H_2O$ flakes over the cathode in the charging process was apparent at early stage of the cycling process. But such flakes were not thoroughly dissolved, and their residuals kept growing in the following cycling process. After 5000 cycles, these flakes were still remained even though the cathode was fully charged, as shown in Figures 5(f) and S14. It can be seen that the eventual sizes of flakes are about 70 μm. EDS mappings for these flakes reveal evenly distributed Zn, S, and O, as shown in Figures 5(g–i), respectively. Further work for tackling the flake-shaped byproducts could start with additives in the $ZnSO_4$ electrolyte.

Conclusion

In summary, aqueous Zn-ion hybrid energy storage devices were fabricated using a composite cathode material, poly(4,4'-TDA)/AC, which resulted in high capacity up to 181.3 mAh g^{-1}. The redox-active poly(4,4'-TDA) plays a key role in enhancing the capacity and shows capacity retention of 83% after 5000 cycles. Different zinc salts were used to make electrolytes and their influences on the formation of byproducts and cycling performance of the cell were studied. It is found that $ZnSO_4$ is the best one for rendering high electrochemical performance, compared to $Zn(CF_3SO_3)_2$. Maximum gravimetric energy and power densities of 203 Wh kg^{-1} and 2.5 kW kg^{-1}, respectively, were achieved. Also, bending performance of a thin and flexible pouch cell was tested, which showed stable capacity when being repeatedly bent and flattened. Our study suggests a new approach to making high-performance Zn-ion

energy storage devices through the combination of nanoporous AC and polymer cathode materials.

Experimental Section

Preparation of the cathode

The 4,4'-thiodianiline (TDA) monomer material was purchased from Shanghai Aladdin Bio-Chem Co., Ltd. and used as received. The nanoporous AC was the YP-80 product from Kuraray Co., Ltd. and was directly used without further treatment. To prepare the cathode, a slurry was made by dispersing AC powder, carbon black, and polyvinylidene fluoride at a weight ratio of 8:1:1 into N-methyl-2-pyrrolidone solvent. The slurry was then coated onto a piece of carbon fiber cloth and the coating area was about 2 cm^{-2}. After a drying process, the AC-coated carbon cloth was put into a three-electrode cell filled with an acidic solution dissolved with 0.03 M 4,4'-TDA (Figure S1a). A platinum foil was used as the counter electrode. With using the Ag/AgCl reference electrode, the electropolymerization process was started by running cyclic voltammetry (CV) test at 20 mV s^{-1} within the voltage window of -0.2–0.65 V for 250 cycles. Optical photographs in Figure S1b show the color evolution of electrolyte in the three-electrode cell during the lelctropolymerization process. The solution dissolved with 4,4'-TDA was initially clear, then gradually turned into dark purple color with increasing the electrodeposition time. The evolution of CV loop with cycling the CV test for electropolymerization is shown in Figure S2. Finally, the obtained poly(4,4'-TDA)/AC electrode was rinsed using deionized water and then dried in a vacuum oven at 80°C overnight. The amount of deposited poly(4,4'-TDA) was weighed using an analytical balance.

Materials characterization

SEM (Zeiss Supra55) and TEM (JEOL-2100F) were employed to study the morphology of electrodes. The EDS elemental mappings were collected on TecnaiG2 20ST (T20) at an acceleration voltage of 100 kV. XPS measurements were carried out on a Thermo Scientific ESCALAB 250Xi instrument with monochromatic Al Kα radiation ($hv = 1486.6$ eV) at ultrahigh vacuum (below 10^{-8} Pa).

Device fabrication

The structure of a Zn-ion hybrid supercapacitor is illustrated in Figure S3(a). Both cathode and separator are soaked with 2 M $ZnSO_4$. The assembled device was sealed into a flat pouch using hot-melting glue, as shown in Figure S3(b).

Electrochemical measurements

The electrochemical measurements of Zn||poly(4,4'-TDA)/AC cell were performed on an electrochemical workstation (CorrTest CS310). GCD tests were performed on a LAND CT3001A battery testing system at room temperature.

The energy in mAh was deduced from the discharge curve in a GCD cycle, as

$$E = \frac{I}{3600} \times \int_{0.2}^{1.8} Vdt = \frac{IS}{3600},$$

where S is the enclosed area between discharge curve and coordinate axis. The average power can be calulated as

$$p = E/t,$$

where t is the time for full discharge.

Acknowledgements

Conflict of Interest

The authors declare no conflict of interest.

Data Availability Statement

The data that support the findings of this study are available in the supplementary material of this article.

[1] M. Li, J. Lu, Z. Chen, K. Amine, *Adv. Mater.* **2018**, *30*, 180056133.
[2] L. F. Xiao, H. Y. Lu, Y. J. Fang, M. L. Sushko, Y. L. Cao, X. P. Ai, H. X. Yang, J. Liu, *Adv. Energy Mater.* **2018**, *8*, 1703238.
[3] Y. X. Zeng, X. Y. Zhang, Y. Meng, M. H. Yu, J. N. Yi, Y. Q. Wu, X. H. Lu, Y. X. Tong, *Adv. Mater.* **2017**, *29*, 1700274.
[4] Y. Cao, P. Zuo, S. Lou, Z. Sun, Q. Li, H. Huo, Y. Ma, C. Du, Y. Gao, G. Yin, *J. Mater. Chem. A* **2019**, *7*, 6533–6542.
[5] N. Choudhary, C. Li, J. Moore, N. Nagaiah, L. Zhai, Y. Jung, J. Thomas, *Adv. Mater.* **2017**, *29*, 1605336.
[6] B. Boruah, *Energy Storage Mater.* **2021**, *34*, 53–75.
[7] J. Sun, C. Wu, X. Sun, H. Hu, C. Zhi, L. Hou, C. Yuan, *J. Mater. Chem. A* **2017**, *5*, 9443–9464.
[8] H. J. Zhang, Y. K. Wang, L. B. Kong, *Nanoscale* **2019**, *11*, 7263–7276.
[9] C. Sun, X. Zhang, C. Li, K. Wang, X. Z. Sun, Y. W. Ma, *Energy Storage Mater.* **2020**, *24*, 160–166.
[10] S. Natarajan, Y. S. Lee, V. Aravindan, *Chem. Asian J.* **2019**, *14*, 936–951.
[11] J. Cao, H. Xu, J. Zhong, X. Li, S. Li, Y. Wang, M. Zhang, H. Deng, Y. Wang, C. Cui, M. Hossain, Y. Cheng, L. Fan, L. Wang, T. Wang, J. Zhu, B. Lu, *ACS Appl. Mater. Interfaces* **2021**, *13*, 8497–8506.
[12] G. Sun, H. Yang, G. Zhang, J. Gao, X. Jin, Y. Zhao, L. Jiang, L. Qu, *Energy Environ. Sci.* **2018**, *11*, 3367–3374.
[13] L. Dong, X. Ma, Y. Li, L. Zhao, W. Liu, J. Cheng, C. Xu, B. Li, Q. Yang, F. Kang, *Energy Storage Mater.* **2018**, *13*, 96–102.
[14] P. Zhang, Y. Li, G. Wang, F. Wang, S. Yang, F. Zhu, X. Zhuang, O. G. Schmidt, X. Feng, *Adv. Mater.* **2018**, *31*, 1806005.
[15] Q. Yang, Z. Huang, X. Li, Z. Liu, Z. Liu, H. Li, G. Liang, D. Wang, Q. Huang, S. Zhang, S. Chen, C. Zhi, *ACS Nano* **2019**, *13*, 8275–8283.
[16] B. Boruah, B. Wen, S. Nagane, X. Zhang, S. Stranks, A. Boies, M. Volder, *ACS Energy Lett.* **2020**, *5*, 3132–3139.
[17] B. Boruah, A. Mathieson, B. Wen, C. Jo, F. Deschler, M. Volder, *Nano Lett.* **2020**, *20*, 5967–5974.
[18] V. Augustyn, P. Simon, B. Dunn, *Energy Environ. Sci.* **2014**, *7*, 1597–1614.
[19] H. Wang, Z. Yu, M. F. El-Kady, M. Anderson, M. D. Kowal, M. Li, R. B. Kaner, *Energy Storage Mater.* **2019**, *19*, 137–147.
[20] Y. Zhao, J. Liu, N. Wang, Q. Li, M. Hu, *J. Mater. Chem. A* **2018**, *6*, 7566–7572.
[21] M. Zhang, Y. Zhang, W. W. Huang, Q. C. Zhang, *Batteries Supercaps* **2020**, *3*, 476–487.
[22] C. Arbizzani, M. Mastragostino, F. Soavi, *J. Power Sources* **2001**, *100*, 164–170.
[23] M. E. Roberts, D. R. Wheeler, B. B. McKenzie, B. C. Bunker, *J. Mater. Chem.* **2009**, *19*, 6977–6979.
[24] C. Meng, C. Liu, L. Chen, C. Hu, S. Fan, *Nano Lett.* **2010**, *10*, 4025–4031.
[25] X. Liu, R. Luo, P. Mei, X. Zhang, Y. Yang, *Energy Technol.* **2020**, *8*, 2000690.
[26] L. S. Cao, D. Li, E. Y. Hu, J. J. Xu, T. Deng, L. Ma, Y. Wang, X. Q. Yang, C. S. Wu, *J. Am. Chem. Soc.* **2020**, *142*, 21404–21409.
[27] N. Zhang, F. Y. Cheng, Y. C. Liu, Q. Zhao, K. X. Lei, C. C. Chen, X. S. Liu, J. Chen, *J. Am. Chem. Soc.* **2016**, *138*, 12894–12901.
[28] Y. Zhang, F. Wan, S. Huang, S. Wang, Z. Q. Niu, J. Chen, *Nat. Commun.* **2020**, *11*, 2199.
[29] W. Liu, M. S. Song, B. Kong, Y. Cui, *Adv. Mater.* **2017**, *29*, 1603436.
[30] Y. Luan, R. Hu, Y. Fang, K. Zhu, K. Cheng, J. Yan, K. Ye, G. Wang, D. Cao, *Nano-Micro Lett.* **2019**, *11*, 30.
[31] L. Fan, K. Lin, J. Wang, R. Ma, B. Lu, *Adv. Mater.* **2018**, *30*, 1800804.
[32] X. Li, M. Chen, L. Wang, H. Xu, J. Zhong, M. Zhang, Y. Wang, Q. Zhang, L. Mei, T. Wang, J. Zhu, B. Lu, X. Duan, *Nanoscale Horiz.* **2020**, *5*, 1586–1595.
[33] Z. Huang, T. Wang, H. Song, X. Li, G. Liang, D. Wang, Q. Yang, Z. Chen, L. Ma, Z. Liu, B. Gao, J. Fan, C. Zhi, *Angew. Chem. Int. Ed.* **2021**, *60*, 1011–1021.
[34] Z. Huang, A. Chen, F. Mo, G. Liang, X. Li, Q. Yang, Y. Guo, Z. Chen, Q. Li, B. Dong, C. Zhi, *Adv. Energy Mater.* **2020**, *10*, 2001024.
[35] Y. Feng, S. Chen, J. Wang, B. Lu, *J. Energy Chem.* **2020**, *43*, 129–138.
[36] Q. Wang, S. Wang, X. Guo, L. Ruan, N. Wei, Y. Ma, J. Li, M. Wang, W. Li, *Adv. Electron. Mater.* **2019**, *5*, 1900537.
[37] H. Shi, Y. Ye, K. Liu, Y. Song, X. Sun, *Angew. Chem. Int. Ed.* **2018**, *130*, 16597–16601.
[38] F. Wan, L. Zhang, X. Dai, X. Wang, Z. Niu, J. Chen, *Nat. Commun.* **2018**, *9*, 1656.